Physics of Plasmas

# Cold ion energization at separatrices during magnetic reconnection

Cite as: Phys. Plasmas **28**, 032104 (2021); https://doi.org/10.1063/5.0008118
Submitted: 18 March 2020 . Accepted: 12 February 2021 . Published Online: 22 March 2021

I. Zaitsev, A. Divin, V. Semenov, I. Kubyshkin, D. Korovinskiy, J. Deca, Yu. Khotyaintsev, and S. Markidis

Physics of Plasmas ARTICLE scitation.org/journal/php

# Cold ion energization at separatrices during magnetic reconnection

Cite as: Phys. Plasmas **28**, 032104 (2021); doi: 10.1063/5.0008118
Submitted: 18 March 2020 · Accepted: 12 February 2021 ·
Published Online: 22 March 2021



I. Zaitsev,[1] A. Divin,[1,a)] V. Semenov,[1] I. Kubyshkin,[1] D. Korovinskiy,[2] J. Deca,[3,4,5] Yu. Khotyaintsev,[6] and S. Markidis[7]

## AFFILIATIONS

[1]Department of Earth's Physics, St. Petersburg State University, St. Petersburg 198504, Russia
[2]Space Research Institute, Austrian Academy of Sciences, Graz 8042, Austria
[3]Laboratory for Atmospheric and Space Physics (LASP), University of Colorado Boulder, Boulder, Colorado 80303, USA
[4]Institute for Modeling Plasma, Atmospheres and Cosmic Dust, NASA/SSERVI, Mountain View, California 94035, USA
[5]Laboratoire Atmosphères, Milieux, Observations Spatiales (LATMOS), Université de Versailles à Saint Quentin, 78280 Guyancourt, France
[6]Swedish Institute of Space Physics, Box 537, SE-751 21 Uppsala, Sweden
[7]KTH Royal Institute of Technology, SE-100 44 Stockholm, Sweden

[a)]**Author to whom correspondence should be addressed:** a.divin@spbu.ru and andrey.div@gmail.com

## ABSTRACT

Separatrices of magnetic reconnection host intense perpendicular Hall electric fields. The fields are produced by the decoupling of the ion and electron components and are associated with the in-plane electrostatic potential drop between the inflow and outflow regions. The width of these structures is typically less than the ion inertial length, which is small enough to demagnetize ions as they cross the layer. We investigate ion acceleration at separatrices by means of 2D particle-in-cell simulations of magnetic reconnection for two limiting cases: (1) a "GEM-like" setup (here GEM stands for geospace environmental modeling reconnection challenge) with the lobe ion thermal velocity equal to the thermal velocity of the initial current sheet ions, which is comparable to the Alfvén velocity and (2) a "cold" ion setup, in which the temperature of the background lobe ions is 1/100 of the initial current sheet temperature. The separatrix Hall electric field is balanced by the ion inertia term in the cold background simulations. The effect is indicative of the quasi-steady local perpendicular acceleration. The electric field introduces a cross field beam of unmagnetized particles, which makes the ion distribution function strongly non-gyrotropic and susceptible to sub-ion scale instabilities. This acceleration mechanism nearly vanishes in the hot ion background simulations. Our particle-in-cell simulations are complemented by one-dimensional test particle calculations. They show that the hot ion particles experience energy-scattering after crossing the accelerating layer, whereas cold ions are uniformly energized up to the energies comparable to the electrostatic potential drop between the inflow and outflow regions.



## I. INTRODUCTION

Magnetic reconnection is a fundamental plasma process in astrophysical, geospace, and laboratory plasmas that changes the magnetic field topology. The process facilitates the conversion of the stored magnetic energy into kinetic, thermal, and suprathermal particle energy.[1] The majority of theoretical and numerical studies of the Earth's magnetotail reconnection are based on the GEM-like symmetric setup[2] which starts from a plain Harris sheet[3] with a peak density $n_0$ (here GEM stands for geospace environmental modeling reconnection challenge). The setup contains a current sheet of width 0.5–1.0 times the ion inertial length $d_i$ ($= c/\omega_{pi0}$, where $c$ is the speed of light and the ion plasma frequency is evaluated for $n_0$) with a background density of 0.05 $n_0$–0.2 $n_0$. Such conditions reproduce common steady and unsteady reconnection features that have been observed by spacecraft (see, e.g., Hesse *et al.*[4] and references therein for a comprehensive review): Hall fields, multiscale ion and electron diffusion regions (referred to as IDR and EDR, respectively), separatrices, and electron beams. The sizes of the electron[5–7] and ion[8,9] diffusion regions scale as $\sim d_e = c/\omega_{pe0}$ (electron inertial length) and $d_i$ (ion inertial length), respectively.

Separatrices of collisionless magnetic reconnection are known to host intense in-plane Hall electric fields associated with density cavities and narrow magnetized electron jets.[6,10] The width[11,12] of the electric field structure mapping the separatrix is less than one $d_i$. In agreement with a Hall reconnection picture,[5,13–15] the electron streamlines converge to the X-line at the separatrices,[16] unlike the ion streamlines[17] which turn smoothly in the outflow direction. Analytical studies estimate the potential drop there[11,12] to be $\sim B^2/(4\pi ne)$. *In situ* cluster observations confirm the existence of a thin $\lesssim d_i$ layer where the perpendicular electric field is balanced by the Hall term $[\mathbf{J}\times\mathbf{B}]/(nec)$, providing the necessary potential drop.[18,19]

The relative absence of collisions in certain magnetospheric and solar system plasmas makes it possible for populations of very different temperatures and/or chemical compositions to coexist. For example, the keV range hot plasma in the magnetotail plasma sheet[20] and inner magnetosphere[21] houses a significant fraction of cold ions (tens of eVs in plasmasphere and tail lobes) of ionospheric origin. Direct measurements of such a population are generally biased by positive charge accumulated by a spacecraft exposed to sunlight. The detection of the cold plasma component is possible indirectly by analyzing the enhanced plasma wake behind a sunlit positively-charged spacecraft.[22,23] Cold ions (comprising up to 50% of density) are also found inside the central plasma sheet in rare events, such as passing through a solar eclipse when the spacecraft potential turned negative.[24]

Particles with different initial temperatures interact differently with the magnetic reconnection substructures. Studies of the impact of cold ions on the reconnection process speculate on their possibility to drift inside the separatrix region due to their small thermal gyroradius.[23,25] Cold ions may change the reconnection rate,[23] modify the Hall effect,[25–28] introduce new plasma scales,[17] and change the overall energy budget of magnetic reconnection.[29,30] Observations of reconnection events at the dayside magnetopause provide evidence about the suppression of Hall currents on scales where cold ions and electrons stay magnetized, while hot ions are not.[26,31] Kinetic simulations of asymmetric reconnection at the magnetopause show that cold ion populations are capable to maintain a Larmor electric field away from the X-line.[28] Event studies of the reconnection exhaust by MMS (magnetospheric multiscale mission) indicate that 10%–25% of the total energy is spent on ion heating.[30]

Theoretical and numerical studies of cold ion mediated reconnection gained momentum through recent observational advances as the microscale physics was found to be controversial close to the X-line and at the separatrices. On the one hand, very low temperature ions have a relatively short gyroradius and thus are magnetized inside the separatrix region.[23] On the other hand, the intense localized electric fields at the separatrices break the frozen-in constraint for cold ions due to the ion inertia.[8,32] Hence, the way particles interact with Hall fields constitutes a basic topic to understand magnetic reconnection in the presence of cold ions.

In this paper, we present results of 2.5D simulations of magnetic reconnection with different background plasma. Specifically, we compare runs with initially only a cold ion background (hereinafter referred to as "Run Rc") to a reference GEM-like setup ("Run Rh"), focusing on differences in ion energization. We identify processes pertaining to the demagnetization of cold ions and discuss the role of the separatrix Hall electric field in heating the cold ion population. Perpendicular cold ion energization is indeed observed at separatrices due to the electric field gradient.[33,34] In a set of test particle calculations, we show that a cold ion reaches energies comparable to the upper limit given by the available total potential drop.[11,12]

The paper is organized as follows: Sec. II describes the setup and the code used. Section III A presents an analysis of the Hall-scale structures at the separatrices. Section III B studies the ion momentum equation in the Rh and the Rc runs. Section III C discusses the features of the phasespace at the separatrices. Section IV devises a test particle model of ion acceleration, followed by summary and conclusions in Sec. V.

## II. SETUP

We perform 2.5D fully kinetic simulations of antiparallel magnetic reconnection using the implicit particle-in-cell code iPIC3D.[35] The simulations are initialized with two Harris current sheets in a double-periodic configuration. The initial magnetic field is given by

$$B_x(y) = B_0(\tanh\{(y - L_y/4)/\lambda^{(H)}\} - \tanh\{(y - 3L_y/4)/\lambda^{(H)}\} - 1).$$

A small localized perturbation is added[17] at $y = L_y/4$, $x = L_x/2$ to seed magnetic reconnection at the center of the current sheet. The plasma density profile that includes the Harris layer component is given by

$$n^{(e,i)H}(y) = n_0(\cosh^{-2}\{(y - L_y/4)/\lambda^{(H)}\} + \cosh^{-2}\{(y - 3L_y/4)/\lambda^{(H)}\})$$

and a uniform background component $n^{(e,i)b}(y) = 0.5n_0$. Here, the superscripts $H$ and $b$ refer to the Harris and background populations, respectively. The Harris layer half thickness is $\lambda^{(H)} = 0.5\ d_i$. The iPIC3D code treats the background and Harris sheet particles as separate species. We investigate the temperature dependence of ion acceleration at the separatrices by performing two runs:

- Run Rh. The reference run. The temperature of the background species (ions, electrons) equals that of the initial Harris component: $T^{(ib)} = T^{(iH)}$, $T^{(eb)} = T^{(eH)}$ with an electron-to-ion temperature ratio of $T^{(eH)}/T^{(iH)} = 1/5$. The computational domain measures $L_x \times L_y = 96d_i \times 24d_i$ and is resolved by $3456 \times 864$ grid cells. Thermal ion gyroradius in the field $B_0$ is $\sim 0.64\ d_i = 23\Delta x$.
- Run Rc. The cold ion run. The temperature of the background ions is set to 0.01 times that of the initial Harris component: $T^{(ib)} = 0.01T^{(iH)}$. The electron parameters are identical to Run Rh: $T^{(eH)}/T^{(iH)} = 1/5$, $T^{(eb)} = T^{(eH)}$. The computational domain measures $L_x \times L_y = 106d_i \times 40d_i$ and is resolved by $3840 \times 1440$ grid cells. Cold ion gyroradius in the field $B_0$ is $\sim 0.064\ d_i = 2.3\Delta x$. Unlike a previous study of symmetric cold ion reconnection,[17] we do not include a hot ion background in this run. The lobe ions (originally cold) dominate inside the diffusion region and the exhaust once the Harris current sheet population is reconnected.

The magnetic field and number densities are normalized to $B_0$ (the asymptotic lobe magnetic field) and $n_0$ (the peak Harris current sheet density), respectively. The length scales are normalized to $d_i$. The velocities are expressed in units of the Alfvén speed $V_A$ based on the plasma density $n_0$ and the magnetic field $B_0$. Time is normalized to the inverse ion cyclotron frequency $\omega_{ci}^{-1} = (eB_0/m_ic)^{-1}$. The reduced ion-to-electron mass ratio is $m_i/m_e = 256$, and the speed of light to

Alfvén velocity ratio is $c/V_A = 103$. Ion gyroperiod is resolved by ~8000 time steps. In what follows, the elementary charge and the ion mass in normalized units are simply $e = 1$, $m_i = 1$, respectively. Energy in the simulations is conserved to 3%.

The axes are as follows: the $x$ axis is parallel to the reconnecting magnetic field, the $z$ axis is parallel to the initial current direction, and $y$ completes the right-handed coordinate system. We use double periodic boundary conditions, with the upper ($y > L_y/2$) Harris current sheet initialized without a perturbation.

It is important to note that kinetic simulations containing only low-energy lobe ions (without a hot background) are carried out for the first time. Such setting might occur during lobe reconnection in the terrestrial magnetotail. It is also a key limiting case from a theoretical viewpoint because the initial ion thermal energy is negligible if compared to the energy gain due to magnetic reconnection. Heating and thermalization in such a regime are purely kinetic processes produced by ion beam mixing in the diffusion region and along the separatrices. It requires full particle simulations to resolve the fine details of the ion distribution function.

## III. RESULTS

### A. Hall physics

An overview of the simulations can be found in Fig. 1. The coordinates are centered at $(x_{(.)}, y_{(.)})$, the X-point position. The X-point does not drift and remains close to $(x_{(.)}, y_{(.)}) = (L_x/2, L_y/4)$ for both runs. Times $t = 36.375$ (Run Rc) and $t = 46.56$ (Run Rh) are selected because the particle data are available for that particular time step. The exhaust contains only the background ion population by these times.

The initial current sheet is pushed away by propagating pileup fronts (the reconnected flux leading edge). These fronts are located at, respectively, $|x - x_{(.)}| \sim 14$ (Run Rc) and $|x - x_{(.)}| \sim 20$ (Run Rh). The fronts propagate with a velocity close to $V_A$ and spread the reconnection electric field in the outflow direction.[36–38] We define the triangle-like region bounded by the separatrices and a front as the "exhaust."[39] "Distant" separatrices are those ahead of the front.

The quadrupolar structure of the $B_z$ component is the main signature of Hall physics in antiparallel reconnection, indicating a decoupling of ions and electrons as they traverse the reconnection region. The $B_z$ field is evident in Figs. 1(a) and 1(f), reaching ~0.37 and ~0.32 in the cold and hot ion background simulations, respectively. The $B_z$ component (and the corresponding Hall electric field $E_y$) reconnection signal[40,41] propagates as a strongly oblique kinetic Alfvén wave (KAW) ($k_\parallel \ll k_\perp$) with a parallel propagation velocity comparable to $\sim\sqrt{(T_e + T_i)/m_e}$. This reduces to $\sqrt{T_e/m_e}$ if $T_i \ll T_e$ and, hence, is similar in runs Rh and Rc up to a factor of 2. The Hall effect produces an intense electric field $E_y$ at the reconnection separatrices, which is responsible for the in-plane electrostatic potential drop, $\phi$, between the inflow and the exhaust.[11,12] The distribution

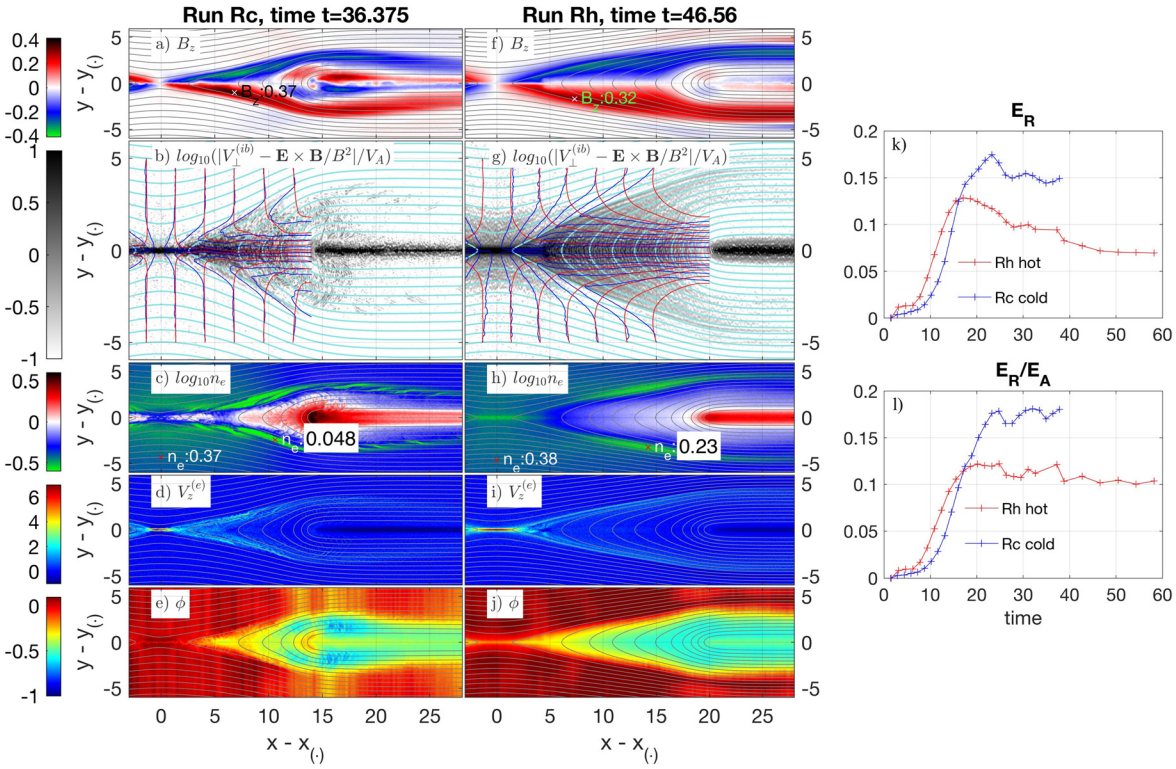


**FIG. 1.** Cold ion background simulation Rc: (a) $B_z$, (b) background: $\log_{10}\{|\mathbf{V}_{perp}^{(ib)} - \mathbf{E}\times\mathbf{B}/B^2|/V_A\}$, electron and background ion streamlines, (c) $\log_{10}n^{(e)}$, (d) $V_z^{(e)}$, (e) in-plane electrostatic potential $\phi$. Hot ion background simulation Rh: (f)–(j) same as (a)–(e). Reconnection rate estimates: (k) $E_R$, (l) $E_R/E_A$, where $E_A = BV_A$ is the instantaneous upstream Alfvén electric field computed at $(x - x_{(.)}, y - y_{(.)}) = (0, 2d_i)$. Datatips in panels (a) and (f) display the peak values of $B_z$. Datatips in panels (c) and (h) display the values of upstream density [$x - x_{(.)} = 0$] and the smallest density inside cavities.

of $\phi$ is quantitatively similar in the Rc [Fig. 1(e)] and the Rh runs [Fig. 1(j)]. Thus, the particles which pass through the separatrix layers should cross nearly the same in-plane potential difference (but not necessarily gain the kinetic energy $\sim|e\phi|$ as we discuss in Sec. IV).

The flow structure is presented in Figs. 1(b) and 1(g). Electron and background ion streamlines are numerically integrated starting from a set of points at $|y - y_{(.)}| = 5$. The integration stops close to the fronts. In both the Rc and the Rh run, the electron streamlines diverge from the ion streamlines toward the X-line[11,12] and generate a Hall current. Qualitatively, the ion flow changes direction smoothly, but the curvature radius of the streamlines at the separatrices is evidently smaller in the Rc run.

To obtain more quantitative information of the ion behavior, we show the normalized perpendicular slippage rate[39,42] $\log_{10}\{|\mathbf{V}_{perp}^{(ib)} - \mathbf{E}\times\mathbf{B}/B^2|/V_A\}$ [the black and white plots in Figs. 1(b) and 1(g)]. Here, $V_A$ is the local Alfvén speed. The measure indicates whether or not the component follows the $\mathbf{E}\times\mathbf{B}$ drift. Regions with intense slippage occupy the exhaust in both the Rc and the Rh run. In the Rc simulation, minor patches of slippage are visible ahead of the fronts.

Plots of the electron density are shown in Figs. 1(c) and 1(h), revealing rather different patterns between the two runs. Past studies of the antiparallel symmetric (see, e.g., Shay *et al.*[6]) and guide-field[10,43] reconnection found long and thin density cavities (or density depletion layers) which map the reconnection separatrices. The depletion layer density in the Rh run is ∼0.23 (compared to ∼0.37 upstream). In the Rc run, we find a much deeper density drop down to ∼0.048, which is approximately an order of magnitude smaller than the upstream plasma density. This result is rather intriguing. The density inside the cavity is controlled by the flux of electrons flowing toward the X-line,[10] but the temperature of ions is involved in the Hall physics as a finite Larmor radius effect. We investigate further in Sec. III B.

The entire reconnection region (diffusion region, exhaust, separatrices, fronts) is perturbed by wave activity: (1) Intense fluctuations inside the EDR might result in the shortening of the EDR current layer in the Rc run [Fig. 1(d)] when comparing with the Rh run [Fig. 1(i)]. (2) Sub-$d_i$ scale density filaments are formed by an instability within several ion inertial lengths near the pileup fronts, which might be due to the fast-streaming reflected cold ion population.[38] Notably, MMS observations of an electrostatic ion–ion beam mode inside a magnetotail reconnection jet have been reported.[44] (3) The density cavities are perturbed by feather-like oblique waves at the exhaust separatrices and distant separatrices. Thus, in the Rc run, cold ions are demagnetized as they flow through the X-line vicinity and the separatrices despite the small thermal ion gyroradius in the upstream plasma. It may seem counter-intuitive that the cold background ion simulation is a much more violent physical process.

The reconnected flux $\Psi$ is estimated as the amount of the magnetic flux trapped between the global X- and the O-lines (more precisely, $\Psi = \int_{x_{(.)}}^{o_{(.)}} B_y(x, L_y/4)dx$). The reconnection rate $E_R$ [Fig. 1(k)] is calculated as the time derivative of $\Psi$ and evolves through two typical stages: (1) the growth phase (during which $E_R$ peaks, $t \sim 17$ for the Rh run and $t \sim 22$ for the Rc run) followed by (2) a quasi-steady phase. Figure 1(l) shows $E_R$ normalized by the local Alfvén electric field calculated at $2d_i$ upstream of the X-point at $x - x_{(.)} = 0$ (to compensate for the density and magnetic flux depletion in the double periodic configuration). A previous study of magnetic reconnection in a mixture of cold (1/5 part) and hot (4/5 part) plasma found a ∼20% increase in $E_R$ in the presence of a cold ion component.[17] According to present simulations, cold ions do not provide a bottleneck and reconnection remains fast in agreement with the idea of ion inertia[5] controlling $E_R$. Figures 1(k) and 1(l) reveal a ∼1.5 times gain in $E_R$ in the cold ion background run despite previous claims[26,45,46] that the suppression of the Hall effect by the $\mathbf{E}\times\mathbf{B}$ drifting cold population would damp $E_R$.

Figure 2 helps us interpret this difference. First we note that the ion outflow velocity $V_{0x}$ has explicit temperature dependence:[47] $V_{0x} = V_A^2/(3\sqrt{T_\parallel^{(i)}/m_i})$, where $V_A$ is the Alfvén speed based on the upstream density. We suggest that $V_{0x}$ limits the reconnection rate because the $z$ component of the ion momentum equation in the distant exhaust is simply $E_z + V_{0x}B_y \sim 0$.

Mean outflow velocities are shown by dashed lines in Fig. 2(a) (∼0.75, Run Rc) and Fig. 2(f) (∼0.45, Run Rh). Shown in datatips in Figs. 2(b) and 2(g) are mean exhaust temperatures $T_\parallel^{(i)}$ for Run Rc (∼0.17) and Run Rh (∼0.66), respectively. Mean temperatures are computed as $\langle T_\parallel^{(i)}\rangle = \langle nT_\parallel^{(i)}\rangle/\langle n\rangle$, where $\langle\ldots\rangle$ denotes averaging over the exhaust center bounded by magnetic separatrices [see Figs. 2(b) and 2(g)]. Indeed, the outflow velocity in the Rc run is larger by a factor of $0.75/0.45 \sim 1.66$ which is in reasonable agreement with the temperature ratio: $\sqrt{0.66/0.17} \sim 1.97$; and reconnection rate ratio in the Rc and Rh runs: $0.15/0.1 \sim 1.5$. Here, $T_\parallel = \mathbf{b}\ddot{\mathbf{T}}\mathbf{b}$ is the temperature parallel to the local magnetic field direction provided by $\mathbf{b} = \mathbf{B}/|\mathbf{B}|$. The gyrotropic perpendicular temperature is $T_\perp = (T_{\perp1} + T_{\perp2})/2 = (Tr(\ddot{\mathbf{T}}) - T_\parallel)/2$. The perpendicular temperatures $T_{\perp1}$, $T_{\perp2}$ are calculated based on the algorithm by Scudder and Daughton.[48]

Bulk ion heating in the exhaust is described by a model by Drake *et al.*[49] The key element of the model is cancelation of the $\mathbf{E}$ field in the frame of reference moving with the exhaust deHoffman–Teller frame (or outflow velocity $V_{0x}$). Under such assumption, the energy of an ion is conserved as it crosses the separatrix and enters the outflow region, where the original pickup mechanism "turns on." Figures 2(d) and 2(e) display $E_y$, $E_z$ components in Run Rc in the transformed frame moving with the velocity $V_{0x}$. Figures 2(i) and 2(j) display the same for Run Rh. Figures 2(d), 2(e), 2(i), and 2(j) reveal that the $E_z$ (reconnecting) component is indeed small, but the $E_y$ (Hall) component is generally non-negligible at separatrices, which points to local acceleration.

We estimate the energy conversion from fields to particles due to this acceleration by plotting $\mathbf{E}\cdot\mathbf{J}^{(i)}$. Marked by arrows in Fig. 2(c) (Run Rc) are strong enhancements at separatrices, which point to local acceleration of cold ions *before* they enter the exhaust. Integrating $\mathbf{E}\cdot\mathbf{J}^{(i)}$ over these layers gives $\sim 2\times 0.04$ for an interval shown by dashed lines in Fig. 2(c). This value amounts to ∼14% of the total $\mathbf{E}\cdot\mathbf{J}^{(i)}$ there. The number most likely to drop with distance as the exhaust opens downstream. The spatial structure of $\mathbf{E}\cdot\mathbf{J}^{(i)}$ in the Run Rh is relatively uniform throughout the exhaust as shown in Fig. 2(h). There are no well-visible layers of $\mathbf{E}\cdot\mathbf{J}^{(i)}$; hence, we set the integration region width equal to the characteristic thickness of the $E_y$ layer at separatrices. The resulting value [see datatips in Fig. 2(h)] amounts to ∼12% of the total exhaust $\mathbf{E}\cdot\mathbf{J}^{(i)}$.

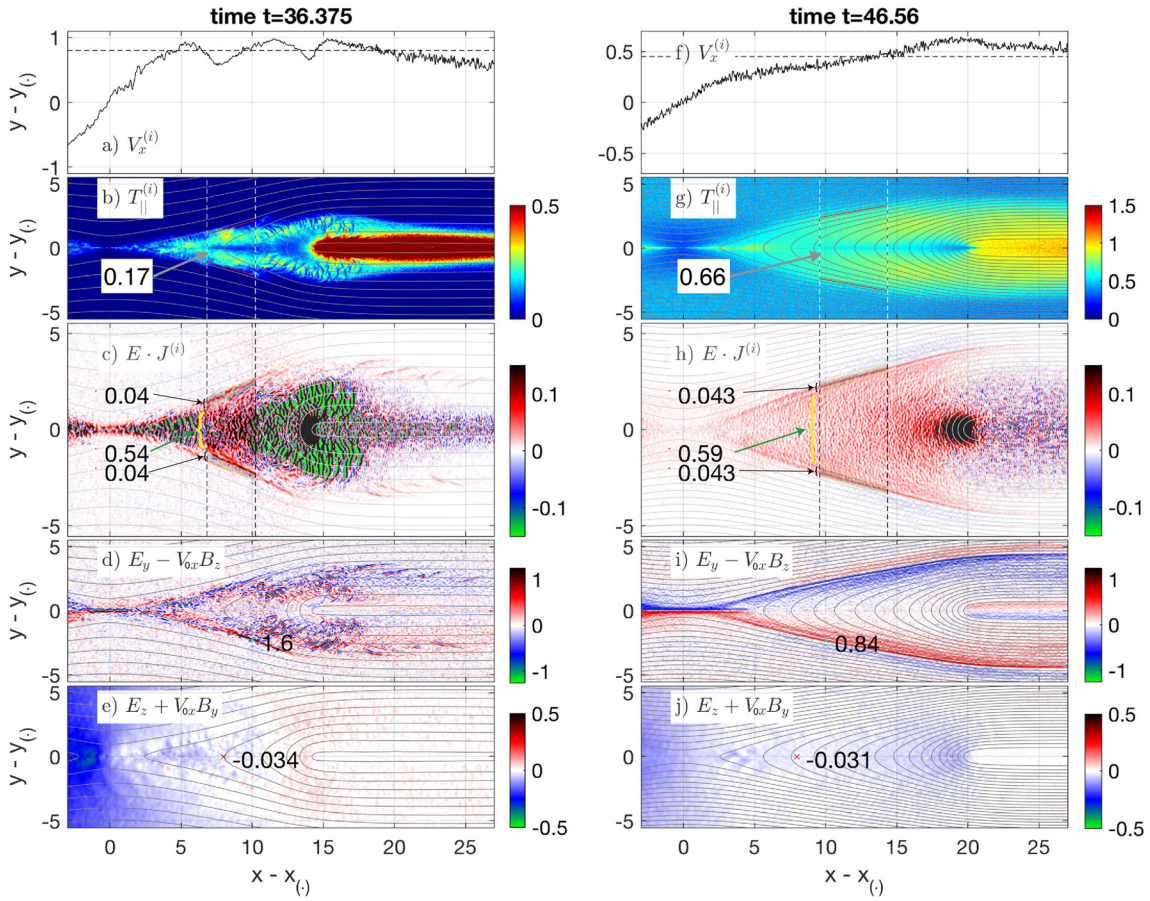


**FIG. 2.** Cold ion background simulation Rc: (a) $V_x^{(i)}$ (solid line), average ion exhaust velocity $V_{0x}$ (dashed line), $y - y_{(.)} = 0$. (b) $T_{||}^{(i)}$. Datatip (0.17) shows the averaged value in the exhaust. (c) $\mathbf{E} \cdot \mathbf{J}^{(i)}$. Datatips show averaged values at the separatrix ($2 \times 0.04$) and in the exhaust (0.54). (d) $E_y$ in a frame moving with the velocity $V_{0x}$. (e) $E_z$ in a frame moving with the velocity $V_{0x}$. Hot ion background simulation Rh: (f)–(j) same as (a)–(e).

Having established the importance of this (pre-) acceleration, we explore next the force balance and particle dynamics in Runs Rc and Rh.

## B. Ion momentum equation

In this section, we investigate the bulk acceleration of the plasma. Figures 3 and 4 display, respectively, the $z$ and the $y$ components of the ion momentum equation

$$\mathbf{E} + \mathbf{V}^{(ib)} \times \mathbf{B} = \frac{1}{en} \nabla \cdot \mathbf{P}^{(ib)} + \frac{m_i}{e} \left( \frac{\partial \mathbf{V}^{(ib)}}{\partial t} + (\mathbf{V}^{(ib)} \cdot \nabla) \mathbf{V}^{(ib)} \right). \quad (1)$$

The $E_z$ component [Figs. 3(a) and 3(e)] is the reconnection electric field. The $E_z$ and the convective component $[\mathbf{V}^{(ib)} \times \mathbf{B}]_z$ [Figs. 3(b) and 3(f)] appear to be the strongest at the pileup fronts, which propagate away from the X-line and push the initial current sheet ions.[38,50] Pileup fronts separate the initial current sheet plasma from the background ion population. The $[\mathbf{V}^{(ib)} \times \mathbf{B}]_z$ and the $E_z$ terms of Eq. (1) are in good balance on large scales and at the fronts in both the Rc and Rh run. The two deviate inside the diffusion region and at the separatrices, where non-ideal effects violate the frozen-in condition.

The reconnection separatrices are standing (exhaust region) or time-dependent (distant separatrices) kinetic Alfvén waves[41] (KAW), which carry the Hall $\mathbf{E}$ field provided mostly by the $E_y$ component [Figs. 4(a) and 4(e)]. Only at distant separatrices (the Rc run), we see a good balance between the $E_y$ [Fig. 4(a)] and $[\mathbf{V}^{(ib)} \times \mathbf{B}]_y$ [Fig. 4(b)]. We examine the ion momentum equation (1) and discuss the violation mechanism of the ion frozen-in condition at reconnection separatrices.

The profile through the exhaust ($x - x_{(.)} = 10$ for Run Rc, $x - x_{(.)} = 13.5$ for Run Rh) is denoted as Profile 1. Only background ions are present there. The profile through the remote separatrices ($x - x_{(.)} = 22.4$ for Run Rc, $x - x_{(.)} = 26.6$ for Run Rh) is denoted as Profile 2. This profile crosses the current sheet plasma, which is neglected in Eq. (1). Therefore, only $|y - y_{(.)}| > 1$ cuts are discussed in application to profile 2 (where the initial current sheet plasma density is negligibly small). The gradients in the perpendicular direction are much larger than in the direction parallel to the $\mathbf{B}$ field. Each quantity in panels (c), (d), (g), and (h) of Figs. 3 and 4 is calculated by averaging over 0.5 $d_i$ in the $\mathbf{B}$ field direction to reduce noise, yet the Rc run profiles are perturbed by intense wave activity.

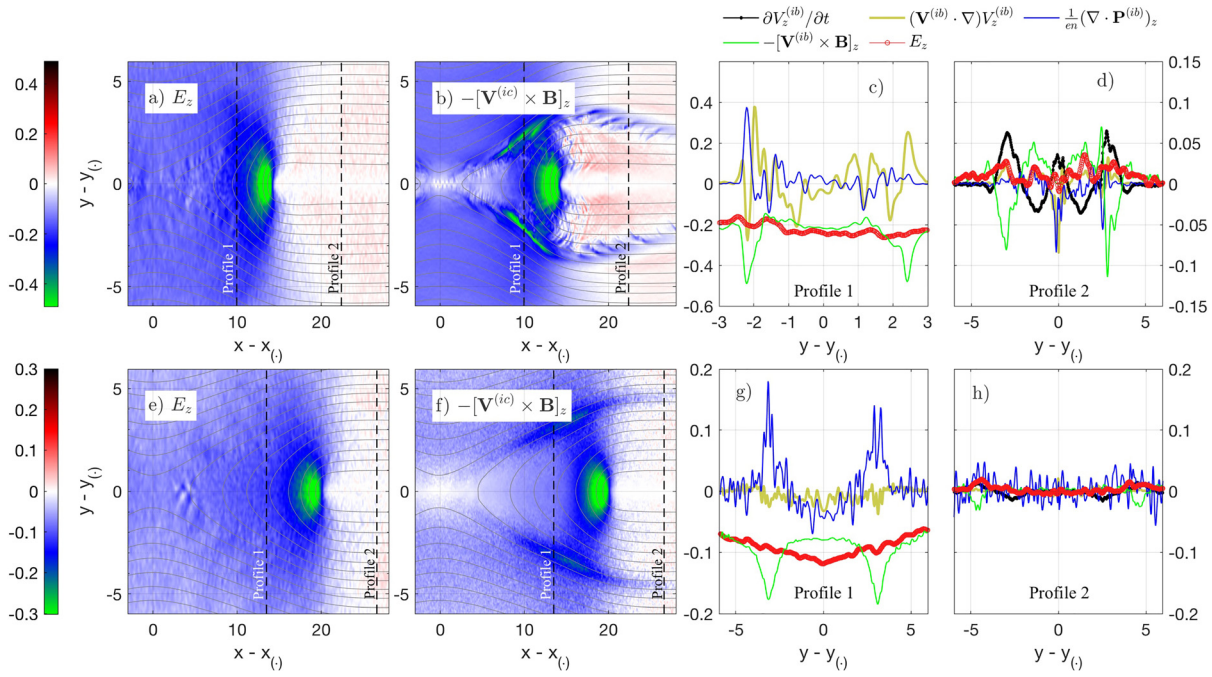


**FIG. 3.** Cold ion background simulation Rc: (a) $E_z$. (b) $-[\mathbf{V}^{(ib)}\times\mathbf{B}]_z$. (c) Terms of the ion momentum equation for a cut through the exhaust (Profile 1). (d) Terms of the ion momentum equation for a cut through the distant separatrices (Profile 2). (e)–(h) Same as (a)–(d), but for the hot ion background run.

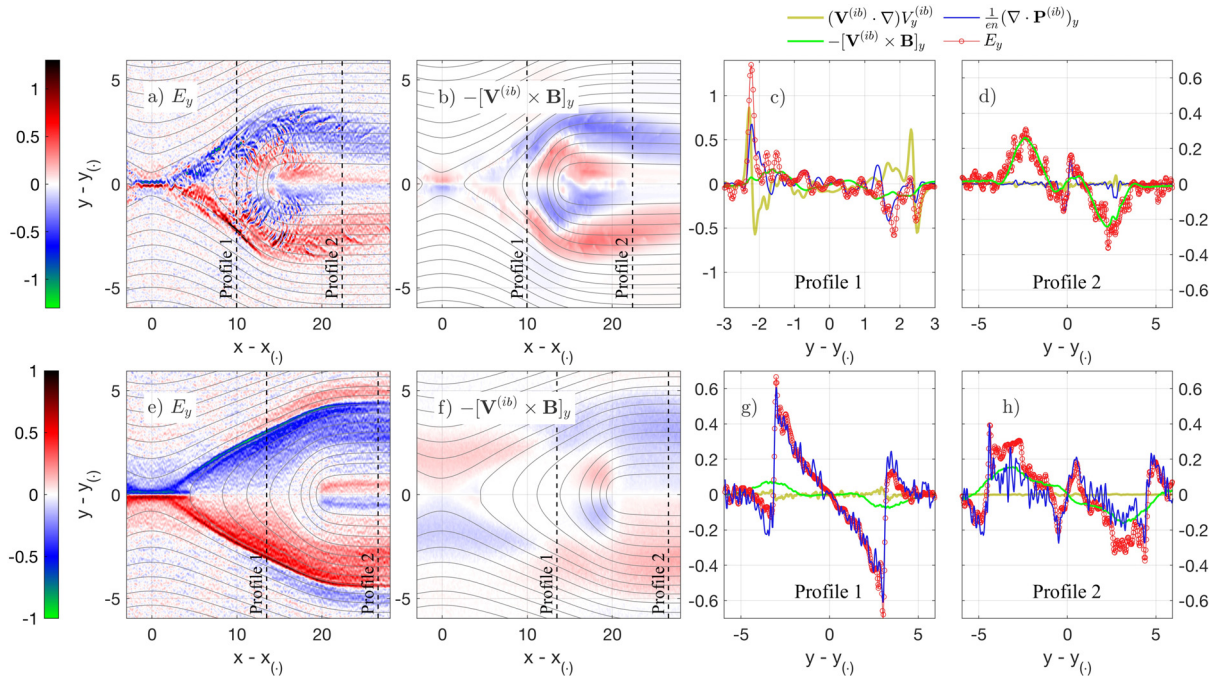


**FIG. 4.** Cold ion background simulation Rc: (a) $E_y$. (b) $-[\mathbf{V}^{(ib)}\times\mathbf{B}]_y$. (c) Terms of the ion momentum equation for a cut through the exhaust. (d) Terms of the ion momentum equation for a cut through the distant separatrices. (e)–(h) Same as (a)–(d), but for the hot ion background run.

The strong pressure gradient and the $E_y$ field are nearly in balance for profile 1 in the Rh run [Fig. 4(g)] in agreement with past hybrid simulations.[51] In the Rc run, the $E_y$ component is of comparable magnitude as the $(\mathbf{V}^{(ib)}\cdot\nabla)\mathbf{V}^{(ib)}$ term at the inflow separatrix edge [visible particularly well at $y-y_{(.)}=2.6$, $y-y_{(.)}=-2.4$ in Fig. 4(c)]. This fact points to a strong local acceleration of cold ions by the Hall electric field in this region. As we will see in Sec. III C, these ions mix with the exhaust ions at the downstream edge, producing strong non-gyrotropic distribution functions; hence, the term $(1/en)\nabla\cdot\mathbf{P}^{(ib)}$ spikes. The convection term $[\mathbf{V}^{(ib)}\times\mathbf{B}]_y$ remains small at the exhaust separatrices in both the Rc and Rh runs [Figs. 4(c) and 4(g)] because the cold ion component cannot $\mathbf{E}\times\mathbf{B}$ drift in such localized electric field as the ions are demagnetized.

The local acceleration by $E_y$ is responsible for an overshoot of $[\mathbf{V}^{(ib)}\times\mathbf{B}]_z\sim -V_y^{(ib)}B_x$ at exhaust separatrices (profile 1 in Fig. 3). The overshoot is due to the ion inertia and pressure terms in run Rc [that is, ion flows are accelerated locally by the electric field of KAWs, see Fig. 3(c)]. In the Rh run, only $(1/en)\nabla\cdot\mathbf{P}^{(ib)}$ balances the overshoot of $[\mathbf{V}^{(ib)}\times\mathbf{B}]_z$ at the separatrices [Fig. 3(g)], pointing again to weaker local acceleration in the hot ion background case.

Distant separatrices are peculiar because the strong Hall $E_y$ signal propagates through background ions which are initially at rest. Both reconnection component $E_z$ and $[\mathbf{V}^{(ib)}\times\mathbf{B}]_z$ [Figs. 3(d) and 3(h) for profiles 2] are negligible outside of the layer at $(|y-y_{(.)}|>5)$. Figure 4(d) reveals that the cold ion velocity is mostly due to the $\mathbf{E}\times\mathbf{B}$ drift; hence, with good accuracy, cold ions can be considered magnetized at the distant separatrix region as discussed by André and Cully.[23]

The localized overshoot in the convective term $[\mathbf{V}^{(ib)}\times\mathbf{B}]_z\sim -V_y^{(ib)}B_x$ persists at distant separatrices due to localized $E_y$ acceleration. The effect is considerably weaker if compared to the exhaust separatrices in the Rc run [Figs. 3(b) and 3(d)]. The ion inertia $\partial V_z^{(ib)}/\partial t$ is of the same magnitude as the convective term. To the leading order, the KAWs accelerate cold ions in the $\mathbf{z}$ direction by the Lorentz force, and $\partial V_z^{(ib)}/\partial t\sim -V_y^{(ib)}B_x$ with the $V_z^{(ib)}$ reaching $\sim$0.3 at the distant separatrices (not shown). A similar force balance establishes in the Rh run, but is barely visible [Figs. 3(f) and 3(h)].

### C. Ion acceleration

Both the Rc and the Rh run contain layers of intense $E_\perp$ at the separatrices, but the details of the force balance are rather different as discussed in Sec. III B.

First, we analyze the acceleration of cold ions in the Rc run. The $E_y$ component forms a narrow ($\sim$0.3 $d_i$ width) unipolar layer where the bulk acceleration of ions is seen. In the inflow region $(y-y_{(.)}<-2.4)$, the distribution function $f^{(ib)}(V_y)$ is a cold Maxwellian component drifting with the $\mathbf{E}\times\mathbf{B}$ velocity [black line in Fig. 5(a)]. Once cold ions enter the layer, they are accelerated by the strong $E_\perp$ ($\sim E_y$) field on sub-$d_i$ scales. This gives rise to the inertia term seen in Fig. 4(c)

$$\frac{dV_y^{(ib)}}{dt}\sim (V^{(ib)}\cdot\nabla)V_y^{(ib)}=(e/m_i)E_y$$

or written as energy: $m_iV_y^2/2\sim|\phi|$ (assuming boundary condition $\phi=0$ in the inflow region).

Acceleration occurs nearly without thermal dispersion as seen in Fig. 5(a) at $y-y_{(.)}\sim -2.3$ up to an effective velocity $\sqrt{2\phi/m_i}$. Good agreement between $V_y^{(ib)}$ and $\sqrt{2\phi/m_i}$ exists up to $y-y_{(.)}=-2.2$. A qualitatively similar dynamics of cold ions is found in magnetotail reconnection events,[25] where a cold beam (well-separated on the ion energy spectrogram) overlaps with hotter plasma at $\sim 1.2d_i$ deep inside the exhaust.

Downstream of this point ($|y-y_{(.)}|<2.2$), a population of the exhaust particles exists, leading to a reduction of $V_y^{(ib)}$ [Fig. 5(b)]. The cross field cold beam makes the distribution function strongly non-gyrotropic [Fig. 5(c)] in the interval $-2.4<y-y_{(.)}<-1.5$. At $y-y_{(.)}=-2.2$, the ratio $T_{\perp1}^{(ib)}/T_{\perp2}^{(ib)}$ peaks at $\sim$10 and a narrow region of perpendicular anisotropy $(T_\perp^{(ib)}/T_\parallel^{(ib)}>1)$ exists at $-2.3<y-y_{(.)}<-2.2$.

The cold beam mixes deeper inside the exhaust and has an effective velocity $\sqrt{2\phi/m_i}\sim 0.8>V_\perp^{(ib)}\sim 0.25$. The distribution function $f^{(ib)}(V_y)$ relaxes gradually into a more gyrotropic distribution in the interval $-2.4<y-y_{(.)}<-1.5$. The ion velocity lags behind the $\mathbf{E}\times\mathbf{B}$ drift inside this region. The two converge inside the exhaust at $|y-y_{(.)}|<0.5$.

The right hand panels of Fig. 5 display, respectively, $f^{(ib)}(V_y)$, bulk flow velocity and temperature for the Rh run along Profile 1. The $E_y$ component peaks at $|y-y_{(.)}|\sim 3.1$ [Fig. 4(g)] at Profile 1. The $E_y$ field does not introduce any noticeable features in $f^{(ib)}(V_y)$ or in the bulk flow velocity components [Fig. 5(e)] in the Rh run. Comparing Figs. 5(a) and 5(d), one finds similar $\sqrt{2\phi/m_i}$ estimates in the exhaust, but the acceleration of ions at the separatrices is very weak in the Rh simulation.

## IV. ION ENERGIZATION AT SEPARATRICES: HOT VS COLD PARTICLES

The results presented in Secs. III A–III C revealed a number of differences between the Rc and Rh run in the ion dynamics at the separatrices:

- The separatrix layers are wider in the Rh run.
- Rc run: the $E_y$ field at the exhaust separatrix is of the same magnitude as the ion inertia term $(\mathbf{V}^{(ib)}\cdot\nabla)V_y^{(ib)}$, indicating local bulk acceleration of particles [Fig. 4(c)]. The distribution function $f^{(ib)}(V_y)$ contains a cross-field beam, which is overlapped with a population of exhaust particles [Fig. 5(a)].
- Rh run: the $E_y$ field is balanced nearly exclusively by $(1/en)\nabla\cdot\mathbf{P}^{(ib)}$, with $(\mathbf{V}^{(ib)}\cdot\nabla)V_y^{(ib)}\sim 0$ [Fig. 4(g)]. There is neither local bulk acceleration at the separatrices nor are there any beam-like features seen in the distribution function [Fig. 5(d)].

To pinpoint the key differences of the ion energization dynamics between the Rc and Rh run, we study numerically trajectories of ions passing through a thin separatrix channel. We devise a one-dimensional test particle model of ion acceleration in the $\mathbf{E}$, $\mathbf{B}$ fields which quantitatively reproduces that at the separatrices. The model contains (1) a uniform magnetic field and a convective electric field (hereinafter denoted as $B_x$ and $E_z$, respectively); (2) a thin layer of the Hall electric field. We use code units, $B_x=1$, $B_y=0$, $B_z=0$, $E_z=-0.1$. The normal electric field is approximated as $E_y=E_0\exp(-y^2/L^2)$, which corresponds to a potential drop of $\Delta\phi_y=E_0\sqrt{\pi}L$ ($\sim$0.4) across the layer.

We calculate a set of test particle trajectories and study the kinetic energy gain as a function of $L$ and initial thermal velocity $V_{th}^{(i)}$. The initial thermal velocities are $V_{th}^{(i)}=0.5V_A$ (approximately Rh run scenario),

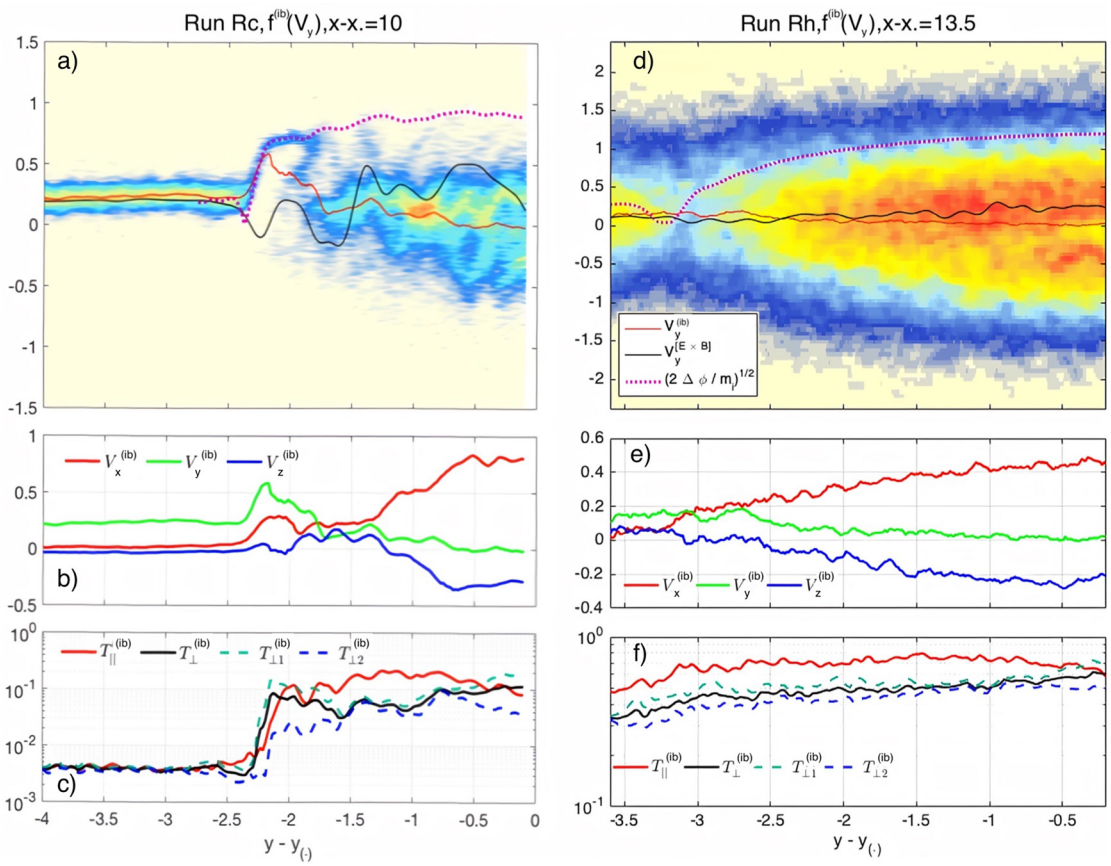


**FIG. 5.** A cut through the exhaust ($x - x_{(.)} = 10$), run Rc: (a) Distribution function $f^{(ib)}(V_y)$, lines display the profiles of $V_y^{(ib)}$, $V^{E\times B}$, and effective velocity $\sqrt{2\Delta\phi/m_i}$. (b) Bulk flow velocity. (c) Components of the temperature tensor. [(d)–(f)] Same as [(a)–(c)] for a cut through the exhaust ($x - x_{(.)} = 13.5$), run Rh.

$V_{th}^{(i)} = 0.2V_A$, $V_{th}^{(i)} = 0.05V_A$ (approximately Rc run scenario). We perform calculations for a wider interval of $0.1 < L < 1.5$, in addition to the PIC simulations value of $L \sim 0.3$. For each $L$ and $V_{th}^{(i)}$, we calculate the trajectories for 10 particles which are initially placed at $y = 3$ and sampled from a Maxwellian distribution having an initial drift velocity of $V_y^{\mathbf{E}\times\mathbf{B}} = E_z/B_x$. At the end of the calculation, the particles are collected at $y = -3$. The resulting energy gain is presented in Fig. 6 and is computed in the frame of reference moving with the $V^{\mathbf{E}\times\mathbf{B}}$ velocity.

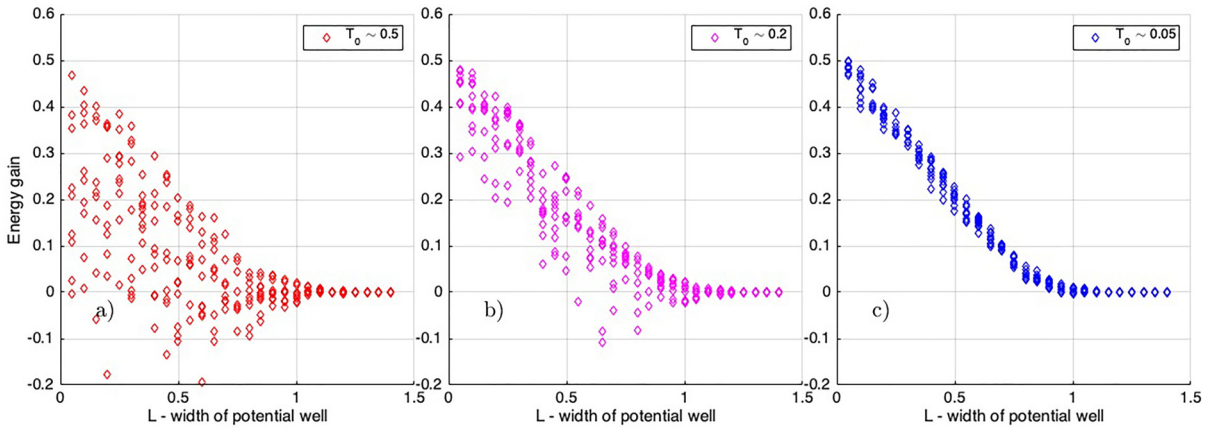


**FIG. 6.** Energy gain vs potential drop width. Initial thermal velocities: (a) $V_{th}^{(i)} = 0.5V_A$; (b) $V_{th}^{(i)} = 0.2V_A$; (c) $V_{th}^{(i)} = 0.05V_A$.

The condition $m_i \nabla E_\perp / eB^2 \sim 1$ introduced by Cole[33] marks a point in the parameter space that divides accelerating and non-accelerating regions. This point is approximately $L \sim 0.9 - 1$ for the present parameters. Both hot and cold ions remain magnetized with little to no kinetic energy change for $L > 1$ shown in Fig. 6 (cases of $m_i \nabla E_\perp / eB^2 < 1$). Opposite to that, a sufficiently thin layer acts as an accelerator of cold ions and an effective scatterer of hot ions.[52] For $L < 1$ (cases of $m_i \nabla E_\perp / eB^2 > 1$), the hot particle distribution represents a wide range of final energies after the crossing [Fig. 6(a)]. The cold particle distribution does not show scattering, with cold ions being uniformly accelerated into the cross field direction.

The test particle simulation results allow us to contrast the three typical cases which are shown in more detail in Fig. 7: (1) cold ion case and a thick layer (left panels), (2) cold ion case and a thin layer (central panels), (3) hot ion case (right panels). An ion passing through the accelerating potential $\phi_y$ would obtain an energy kick of $\sim e\Delta\phi_y$ (red lines in bottom panels). However, the $E_z$,$B_x$ components pull the particle in the $z$-direction [see the trajectories in Figs. 7(b), 7(f), and 7(j)] and introduce the change in $\Delta\phi_z = \int E_z dz$ of the opposite sign (green lines in the three bottom panels in Fig. 7). Therefore, the resulting energy gain $\Delta\phi_y + \Delta\phi_z$ relies on the competition between those two [see Figs. 7(d), 7(h), and 7(l)], which in turn depends on the degree of magnetization of a particle.

An apparent result here is that when the width of the potential drop is much larger than a particle's gyroradius, the particle remains magnetized and moves in the $\mathbf{E} \times \mathbf{B}$ direction. No energy gain occurs in such a case, because $\Delta\phi_y + \Delta\phi_z \sim 0$. Such a regime might occur during predominantly hot ion reconnection when the cold ions are present as minor species. If the electric field layer width is comparable to or less than the gyroradius, the drift theory is no longer applicable and the energy gain depends on the thermal velocity. If the thermal velocity is less than $V^{\mathbf{E}\times\mathbf{B}}$ (which is the case of cold ions), the particle will acquire additional perpendicular energy [Fig. 7(g)].

The regime $m_i \nabla E_\perp / eB^2 > 1$ is neglected in the original Drake *et al.*[49] model, which assumes that a particle's velocity is unchanged as it crosses the separatrix transition layer. According to the model, the layer width controls dynamics of ions in the exhaust:

- Large gyroradius particles (e.g., heavy ions) experience pickup acceleration.
- Particles having a small radius (e.g., cold protons) remain adiabatic and magnetized while passing through the transition layer. Such particles start drifting with $V^{\mathbf{E}\times\mathbf{B}}$ velocity and undergo bounce motions across the midplane of the exhaust.

This approach might be applicable in large guide field limit since the transition layer width scales as the gyroradius at ion sound velocity.[53] However, for antiparallel magnetic reconnection, the transition layer width is comparable to a few electron inertial lengths $\sim (m_e/m_i)^{1/2}$ and gets rather thin for realistic mass ratio.

Summing up the results of the test particle calculations, we conclude that the behavior of an ion crossing the separatrix depends crucially on its thermal gyroradius. The perpendicular velocity of cold

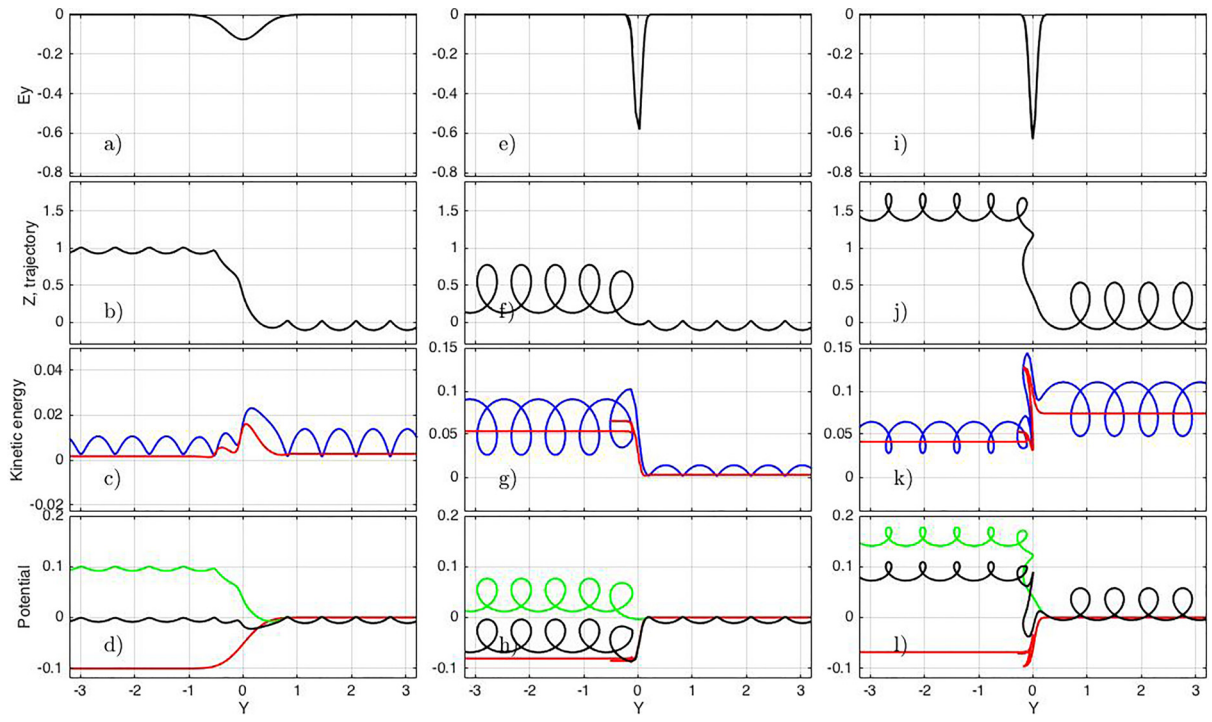


**FIG. 7.** Test particle simulation results for three typical cases: [(a)–(d)] smooth gradient $\frac{\partial E_y}{\partial y}$ (left column), [(e)–(h)] acceleration on a sharp gradient affecting on cold particle (central column), [(i)–(l)] deceleration on a sharp gradient affecting on hot particle (right column). From top to bottom: [(a), (e), and (i)] shape of electric field inhomogeneity, [(b), (f), and (j)] particle trajectory in cross field plane Y-Z, [(c), (g), and (k)] energy gain [total kinetic energy gain (blue), kinetic energy gain in $[E \times B]$ drifting system (red)], [(d), (h), and (l)] evolution of the electrostatic potential (black) and the following terms along trajectory: $\Delta\phi_y = -\int E_y dy$ (red) and $\Delta\phi_z = -\int E_z dz$ (green).

ions increases sharply in the Rc run, in a narrow region where the drift theory is violated. The hot ions (third column in Fig. 7) passing through the same electrostatic potential drop are scattered in the Rh run, with a peak energy gain amounting to a potential drop $\phi$, which is in turn comparable in the Rc and Rh run.

## V. SUMMARY AND CONCLUSIONS

We investigated the acceleration and heating of cold ions during the process of collisionless antiparallel symmetric reconnection. Comparing the simulation results to a reference run with hot ions (GEM-like setup[2]), we found rather similar large-scale reconnection structures and basic properties. More specifically, magnetic reconnection is fast with reconnection rates up to ~0.1 but shows explicit upstream ion temperature dependence, in agreement with Haggerty *et al.*[47] Reconnection jet fronts are formed at the initial stage of the process in both runs, and ions and electrons are decoupled inside the diffusion region and at the separatrices. Notable differences appear when considering small-scale kinetic effects.

The patterns and magnitudes of the quadrupolar magnetic field $B_z$ [Figs. 1(a) and 1(f)] and the Hall electric field $E_y$ [Figs. 4(a) and 4(e)] are rather similar in the Rc and Rh run inside the quasi-steady exhaust region (with $E_y$ being noisier in the Run Rc due to wave activity). However, substantial differences are found in the ion force balance at the separatrices. The Hall electric field $E_y$ is balanced only by the ion pressure term in the hot ion simulation in agreement with past studies.[51] The cold ion run shows the presence of a strong inertial term $(\mathbf{V}^{(ib)} \cdot \nabla) V_y^{(ib)}$ at the separatrices because the inflowing population has no thermal motion (cf. results of Fujimoto and Takamoto[54] featuring a low-density plasma with thermal velocity much smaller than the local Alfvén velocity). The ion pressure term becomes dominant deeper inside the exhaust in Run Rc, indicating thermalization of the cold ion population and the corresponding increase in the ion pressure.

Magnetic reconnection separatrices can be roughly divided into two regions:

(1) Close to the diffusion region (between the X-line and the pileup front), the exhaust separatrices are standing whistler or kinetic Alfvén waves[40,55]
(2) Far from the diffusion region (ahead of the front), the separatrices are oblique kinetic Alfvén waves[41] produced by fast parallel electron flows.

Both regions host a strong Hall $E_y$ signature, but the closer region (1) also contains the reconnection electric field $E_z$. The latter component appears crucial for the cold ion energization at the separatrices because $E_z$ drives ions toward the exhaust. When a cold ion crosses the $E_y$ field layer far from the diffusion region (region 2), in the absence of $E_z$ it will experience the $\mathbf{E} \times \mathbf{B}$ drift motion that might lead to perpendicular current reduction.[31] However, when crossing the exhaust separatrices case (region 1), the magnetic moment of cold ions grows rapidly. Such a pre-heated population forms a cross field beam entering the exhaust. Our simulations display a qualitative agreement with an event study of magnetotail reconnection,[25] where cold beams were found ~1.2 $d_i$ deep inside the exhaust without thermalization.

We proposed a model which includes a uniform reconnection electric field and a localized Hall electric field that has a gradient perpendicular to both the **B** field direction and the uniform **E** component. Test particle calculations show that ions crossing the separatrices are energized[33] if $m_i \nabla E_\perp / eB^2 > 1$. Cold ions (Run Rc) are uniformly accelerated into the cross field direction, whereas hot ions (Run Rh) experience scattering in energies. However, if $m_i \nabla E_\perp / eB^2 < 1$, then the kinetic energy of ions is conserved. We suggest that the latter regime is considered in the model by Drake *et al.*,[49] which provides predictions of ion heating neglecting the (pre-)acceleration at reconnection separatrices. The energy available per particle that goes to heating[56,57] is $\sim \alpha m_i V_A^2$ where the fraction is $\alpha = 0.1 - 0.2$. Surprisingly, this number is comparable in the Rc and Rh run[17] despite differences in the separatrix heating processes. Hence, the questions remain: (1) whether the ion energy gain during magnetic reconnection $\sim \alpha m_i V_A^2$ is universal for different acceleration mechanisms and (2) what is the background temperature dependence. We hypothesize the spacecraft measurements would help to solve these outstanding issues.

## ACKNOWLEDGMENTS

This research was partially funded by Russian Foundation for Basic Research (RFBR) Project No. 20–55-53011 and the Austrian Science Fund (FWF): I 3506-N27. A.D. (I.Z.) acknowledges the financial support by the Programme Metchnikov (Ostrogradsky) 2019 for a short stay visit at École polytechnique, Paris. The work was supported by the Foundation for the Advancement of Theoretical Physics and Mathematics "BASIS," Grant No. 20–1-2–18-1. Simulation were conducted on the resources of KTH, Stockholm (Sweden, Project Nos. 2016/1–457 and 2018/3–95 and 2019–3-128) and MSU, at Lomonosov supercomputing facility Project Nos. 1576, 1658, Moscow (Russia).

## DATA AVAILABILITY

The data that support the findings of this study are available from the corresponding author upon reasonable request.

## REFERENCES

[1] E. R. Priest and T. Forbes, *Magnetic reconnection: MHD Theory and Applications* (Cambridge University Press, 2000), p. 600.
[2] J. Birn, J. F. Drake, M. A. Shay, B. N. Rogers, R. E. Denton, M. Hesse, M. Kuznetsova, Z. W. Ma, A. Bhattacharjee, A. Otto, and P. L. Pritchett, J. Geophys. Res. **106**, 3715, https://doi.org/10.1029/1999JA900449 (2001).
[3] E. G. Harris, Il Nuovo Cimento (1955–1965) **23**, 115 (1962).
[4] M. Hesse, N. Aunai, J. Birn, P. Cassak, R. Denton, J. Drake, T. Gombosi, M. Hoshino, W. Matthaeus, D. Sibeck *et al.*, Space Sci. Rev. **199**, 577 (2016).
[5] D. Biskamp, E. Schwarz, and J. Drake, Phys. Rev. Lett. **75**, 3850 (1995).
[6] M. A. Shay, J. F. Drake, B. N. Rogers, and R. E. Denton, J. Geophys. Res. **106**, 3759, https://doi.org/10.1029/1999JA001007 (2001).
[7] A. Divin, G. Lapenta, S. Markidis, V. S. Semenov, N. V. Erkaev, D. B. Korovinskiy, and H. K. Biernat, J. Geophys. Res.: Space Phys. **117**, A06217 (2012), https://doi.org/10.1029/2011JA017464.
[8] A. Ishizawa and R. Horiuchi, Phys. Rev. Lett. **95**, 045003 (2005).
[9] P. Wu, M. A. Shay, T. D. Phan, M. Oieroset, and M. Oka, Phys. Plasmas **18**, 111204 (2011).
[10] J. F. Drake, M. A. Shay, W. Thongthai, and M. Swisdak, Phys. Rev. Lett. **94**, 095001 (2005).
[11] D. B. Korovinskiy, V. S. Semenov, N. V. Erkaev, A. V. Divin, and H. K. Biernat, J. Geophys. Res.: Space Phys. **113**, 4205 (2008), https://doi.org/10.1029/2007JA012852.
[12] D. B. Korovinskiy, V. S. Semenov, N. V. Erkaev, A. V. Divin, H. K. Biernat, and U. V. Möstl, J. Geophys. Res.: Space Phys. **116**, A05219 (2011), https://doi.org/10.1029/2010JA015942.

[13]D. A. Uzdensky and R. M. Kulsrud, Phys. Plasmas **13**, 062305 (2006).
[14]B. U. Ö. Sonnerup, *Magnetic Field Reconnection*, Solar System Plasma Physics, edited by L. T. Lanzerotti, C. F. Kennel, and E. N. Parker (North-Holland, New York, 1979), Vol. 3, p. 45.
[15]T. Terasawa, Geophys. Res. Lett. **10**, 475, https://doi.org/10.1029/GL010i006p00475 (1983).
[16]M. Hoshino, T. Mukai, T. Terasawa, and I. Shinohara, J. Geophys. Res.: Space Phys. **106**, 25979, https://doi.org/10.1029/2001JA900052 (2001).
[17]A. Divin, Y. V. Khotyaintsev, A. Vaivads, M. André, S. Toledo-Redondo, S. Markidis, and G. Lapenta, J. Geophys. Res.: Space Phys. **121**, 12001, https://doi.org/10.1002/2016JA023606 (2016).
[18]Y. V. Khotyaintsev, A. Vaivads, A. Retinò, M. André, C. Owen, and H. Nilsson, Phys. Rev. Lett. **97**, 205003 (2006).
[19]T. Lindstedt, Y. V. Khotyaintsev, A. Vaivads, M. André, R. Fear, B. Lavraud, S. Haaland, and C. Owen, Ann. Geophys. **27**, 4039 (2009).
[20]W. Baumjohann, G. Paschmann, and C. Cattell, J. Geophys. Res.: Space Phys. **94**, 6597, https://doi.org/10.1029/JA094iA06p06597 (1989).
[21]D. Baker, Surv. Geophys. **16**, 331 (1995).
[22]E. Engwall, A. I. Eriksson, C. M. Cully, M. André, P. Puhl-Quinn, H. Vaith, and R. Torbert, Ann. Geophys. **27**, 3185–3201 (2009).
[23]M. André and C. M. Cully, Geophys. Res. Lett. **39**, L03101 (2012), https://doi.org/10.1029/2011GL050242.
[24]K. Seki, M. Hirahara, M. Hoshino, T. Terasawa, R. C. Elphic, Y. Saito, T. Mukai, H. Hayakawa, H. Kojima, and H. Matsumoto, Nature **422**, 589 (2003).
[25]L. Alm, M. André, A. Vaivads, Y. Khotyaintsev, R. B. Torbert, J. L. Burch, R. Ergun, P.-A. Lindqvist, C. T. Russell, B. L. Giles *et al.*, Geophys. Res. Lett. **45**, 11941–11950 (2018), https://doi.org/10.1029/2018GL079857.
[26]S. Toledo-Redondo, A. Vaivads, M. André, and Y. V. Khotyaintsev, Geophys. Res. Lett. **42**, 6146, https://doi.org/10.1002/2015GL065129 (2015).
[27]M. André, W. Li, S. Toledo-Redondo, Y. V. Khotyaintsev, A. Vaivads, D. Graham, C. Norgren, J. Burch, P.-A. Lindqvist, G. Marklund *et al.*, Geophys. Res. Lett. **43**, 6705, https://doi.org/10.1002/2016GL069665 (2016).
[28]J. Dargent, N. Aunai, B. Lavraud, S. Toledo-Redondo, M. Shay, P. Cassak, and K. Malakit, J. Geophys. Res.: Space Phys. **122**, 5290, https://doi.org/10.1002/2016JA023831 (2017).
[29]N. Aunai, G. Belmont, and R. Smets, Phys. Plasmas **18**, 122901 (2011).
[30]S. Toledo-Redondo, M. André, Y. V. Khotyaintsev, B. Lavraud, A. Vaivads, D. B. Graham, W. Li, D. Perrone, S. Fuselier, D. J. Gershman *et al.*, J. Geophys. Res.: Space Phys. **122**, 9396, https://doi.org/10.1002/2017JA024553 (2017).
[31]S. Toledo-Redondo, J. Dargent, N. Aunai, B. Lavraud, M. André, W. Li, B. Giles, P.-A. Lindqvist, R. E. Ergun, C. T. Russell *et al.*, Geophys. Res. Lett. **45**, 10033, https://doi.org/10.1029/2018GL079051 (2018).
[32]A. Ishizawa, R. Horiuchi, and H. Ohtani, Phys. Plasmas **11**, 3579 (2004).
[33]K. Cole, Planet. Space Sci. **24**, 515 (1976).
[34]T. Lindstedt, Y. V. Khotyaintsev, A. Vaivads, M. André, H. Nilsson, and M. Waara, Geophys. Res. Lett. **37**(9), L09103 (2010), https://doi.org/10.1029/2010GL043117.
[35]S. Markidis, G. Lapenta, and R. Uddin, Math. Comput. Simul. **80**, 1509 (2010).
[36]S.-I. Ohtani, M. A. Shay, and T. Mukai, J. Geophys. Res.: Space Phys. **109**, 3210, https://doi.org/10.1029/2003JA010002 (2004).
[37]M. I. Sitnov, M. Swisdak, and A. V. Divin, J. Geophys. Res.: Space Phys. **114**, A04202 (2009), https://doi.org/10.1029/2008JA013980.
[38]P. Wu and M. A. Shay, Geophys. Res. Lett. **39**, L08107 (2012), https://doi.org/10.1029/2012GL051486.
[39]H. Liang, G. Lapenta, R. J. Walker, D. Schriver, M. El-Alaoui, and J. Berchem, J. Geophys. Res.: Space Phys. **122**, 618, https://doi.org/10.1002/2016JA023060 (2017).
[40]J. F. Drake, M. A. Shay, and M. Swisdak, Phys. Plasmas **15**, 042306 (2008).
[41]M. A. Shay, J. F. Drake, J. P. Eastwood, and T. D. Phan, Phys. Rev. Lett. **107**, 065001 (2011).
[42]M. V. Goldman, D. L. Newman, and G. Lapenta, Space. Sci. Rev. **199**, 651 (2016).
[43]G. Lapenta, S. Markidis, A. Divin, M. Goldman, and D. Newman, Phys. Plasmas **17**, 082106 (2010).
[44]C. Liu, A. Vaivads, D. Graham, Y. V. Khotyaintsev, H. Fu, A. Johlander, M. André, and B. Giles, Geophys. Res. Lett. **46**, 12702–12710 (2019), https://doi.org/10.1029/2019GL085419.
[45]M. André, A. Vaivads, Y. V. Khotyaintsev, T. Laitinen, H. Nilsson, G. Stenberg, A. Fazakerley, and J. Trotignon, Geophys. Res. Lett. **37**(22), L22108 (2010), https://doi.org/10.1029/2010GL044611.
[46]S. Toledo-Redondo, M. André, A. Vaivads, Y. V. Khotyaintsev, B. Lavraud, D. Graham, A. Divin, and N. Aunai, Geophys. Res. Lett. **43**, 58–66 (2016), https://doi.org/10.1002/2015GL067187.
[47]C. C. Haggerty, M. A. Shay, A. Chasapis, T. D. Phan, J. F. Drake, K. Malakit, P. A. Cassak, and R. Kieokaew, Phys. Plasmas **25**, 102120 (2018).
[48]J. Scudder and W. Daughton, J. Geophys. Res.: Space Phys. **113**, A06222 (2008), https://doi.org/10.1029/2008JA013035.
[49]J. Drake, M. Swisdak, T. Phan, P. Cassak, M. Shay, S. Lepri, R. Lin, E. Quataert, and T. Zurbuchen, J. Geophys. Res.: Space Phys. **114**, A05111 (2009), https://doi.org/10.1029/2008JA013701.
[50]X.-Z. Zhou, V. Angelopoulos, V. A. Sergeev, and A. Runov, J. Geophys. Res.: Space Phys. **115**, A00I03 (2010), https://doi.org/10.1029/2010JA015481.
[51]N. Aunai, G. Belmont, and R. Smets, J. Geophys. Res.: Space Phys. **116**, A09232 (2011), https://doi.org/10.1029/2011JA016688.
[52]K. Stasiewicz, R. Lundin, and G. Marklund, Phys. Scr. **T84**, 60 (2000).
[53]J. F. Drake, P. Cassak, M. Shay, M. Swisdak, and E. Quataert, Astrophys. J. Lett. **700**, L16 (2009).
[54]K. Fujimoto and M. Takamoto, Phys. Plasmas **23**, 012903 (2016).
[55]B. N. Rogers, R. E. Denton, J. F. Drake, and M. A. Shay, Phys. Rev. Lett. **87**, 195004 (2001).
[56]C. Haggerty, M. Shay, J. Drake, T. Phan, and C. McHugh, Geophys. Res. Lett. **42**, 9657, https://doi.org/10.1002/2015GL065961 (2015).
[57]T. Phan, J. Drake, M. Shay, J. Gosling, G. Paschmann, J. Eastwood, M. Oieroset, M. Fujimoto, and V. Angelopoulos, Geophys. Res. Lett. **41**, 7002, https://doi.org/10.1002/2014GL061547 (2014).